# Transcription factor dimerization activates the p300 acetyltransferase

Esther Ortega, Srinivasan Rengachari, Ziad Ibrahim, Naghmeh Hoghoughi, Jonathan Gaucher, Alex Holehouse, Saadi Khochbin, Daniel Panne

Nature. 2018 Oct;562(7728):538-544. doi: 10.1038/s41586-018-0621-1. Epub 2018 Oct 15.

# Cellular signaling activates the p300 acetyltransferase through transcription factor dimerization

Esther Ortega[1], Srinivasan Rengachari[1], Ziad Ibrahim[1], Naghmeh Hoghoughi[3], Jonathan Gaucher[1], Alex S. Holehouse[4], Saadi Khochbin[3], Daniel Panne[*1, 2]

[1]European Molecular Biology Laboratory, 38042 Grenoble, France.

[2]Leicester Institute of Structural and Chemical Biology, Department of Molecular and Cell Biology, University of Leicester, Lancaster Road, Leicester, LE1 7RH

[3]CNRS UMR 5309, INSERM, U1209, Université Grenoble Alpes, Institute for Advanced Biosciences, 38700 Grenoble, France

[4]Department of Biomedical Engineering and Center for Biological Systems Engineering, Washington University in St. Louis, St. Louis, MO, USA.

[*]Corresponding author: email: daniel.panne@le.ac.uk

**Summary**

The transcriptional coactivator p300 is a histone lysine acetyltransferase that is typically recruited to transcriptional enhancers and regulates gene expression by acetylating chromatin. Here we show that p300 activation directly depends on the activation and oligomerisation status of transcription factor (TF) ligands. Using two model TFs, IRF3 and STAT1, we demonstrate that TF dimerization enables trans-autoacetylation of p300 in a highly conserved and intrinsically disordered autoinhibitory lysine-rich loop (AIL) resulting in HAT activation. We describe a p300 crystal structure in which the AIL invades the active site of a neighboring HAT domain thus revealing a snap-shot of a trans-autoacetylation reaction intermediate. Substrate access to the active site involves rearrangement of an autoinhibitory RING domain. Our data explain how cellular signaling, TF activation and dimerization controls p300 activation thus explaining why gene transcription is associated with chromatin acetylation.

**Keywords**

P300, CBP, acetyltransferase, Chromatin, IRF3, STAT1, transcription factor, transcriptional regulation

## Introduction

Signals that emanate from cellular receptors ultimately lead to changes in gene expression programs that drive cellular change and organismal development. Gene expression is typically controlled through the coordinated activity of DNA-binding transcription factors (TFs), chromatin regulators, and the general transcription machinery. For instance, in the innate immune system, a number of pattern recognition receptors (PRRs) recognize various pathogen-associated molecular patterns (PAMPs)[1]. Once engaged by PAMPs, PRRs bind to adaptor proteins such as STING (stimulator of IFN genes). These adaptor proteins engage the latent DNA binding TF interferon (IFN) regulatory factor 3 (IRF3) and enable recruitment and activation of the non-canonical IKK kinase TBK1[1]. TBK1 then phosphorylates IRF3 in a C-terminal motif, which results in removal of autoinhibition, dimerization and adaptor displacement[2,3]. Activated IRF3 dimers bind to p300/CBP (also known as KAT3B and KAT3A) to stimulate chromatin acetylation and gene expression of antiviral type I IFNs IFN-α and IFN-β[3-5]. Type I IFNs cytokines are secreted and bind to specific cell surface IFN receptors (IFNARs), which results in activation of Janus kinase/signal transducers and activators of transcription (JAK/STAT) signaling[6]. Activated, tyrosine phosphorylated STATs dimerize, translocate to the nucleus and bind to p300/CBP to stimulate transcription of IFN-stimulated genes (ISGs)[7].

p300/CBP are known to interact with more than 400 binding partners including the basal transcription machinery[8]. The large protein interactome of p300/CBP results in near universal recruitment of these histone lysine acetyltransferases (HATs) to enhancers and p300 occupancy has been used to identify enhancers genome-wide[9-11]. CBP/p300 catalyze acetylation of histone H3K27, a modification that is considered an 'activation' mark[12]. However, recruitment of CBP/p300 does not always correlate with gene activation and is occasionally associated with repression[13-17]. A large number of chromatin regions that bind CBP/p300 therefore do not contain this canonical H3K27ac modification, indicating that HAT activity at such sites is blocked[16,18]. Thus a major challenge is to understand the mechanism that allows

switching between inactive and active states of CBP/p300 on enhancers, and to causally link cellular signaling to the recruitment of CBP/p300, regulation of HAT activity and to the establishment of repressed, poised and active chromatin.

Here we have investigated how the activation and oligomerization status of p300 TF ligands such as IRF3 and STAT1 impacts the catalytic activity of p300. We found that the kinase-activated, dimeric and DNA-binding competent form, but not inactive or monomeric variants of these TFs, support robust p300 HAT activation. We demonstrate that IRF3 or STAT1 activation and dimerization enables p300 trans-autoacetylation in a lysine-rich, intrinsically disordered autoinhibitory loop (AIL) in the HAT domain that serves as a 'pseudo-substrate' and is important for the regulation of p300 HAT activity[19]. A crystal structure of the core domain of p300 provides a snapshot of a potential trans- autoacetylation reaction intermediate in which the AIL projects into the active site of a neighboring p300 molecule. Substrate access requires a conformational rearrangement of the autoinhibitory RING domain into a position that results in a more accessible HAT active site. All-atom simulations and biochemical experiments indicate that AIL acetylation and RING domain repositioning regulates dynamic interactions with the HAT substrate binding pocket to regulate HAT substrate access. As HAT activation is intimately linked to TF activation, these results causally relate cellular signaling to the activation and DNA targeting of a chromatin modifier and provide mechanistic insights into the long-standing and general correlation between an active, acetylated chromatin structure and gene transcription.

## Results

### Transcription factor dimerization enables activation of p300

To explore if p300 is activated by signal-dependent IRF3 dimerization, we produced three recombinant IRF3 species: inactive monomers (IRF3), active IRF3 dimers by TBK1 phosphorylation (pIRF3) and a

truncation mutant lacking the C-terminal autoinhibitory element (IRF3ΔC) (Extended Data Fig. 1a, b). Truncation of the C-terminal autoinhibitory element allows CBP/p300 binding but abolishes IRF3 dimerization[20]. We confirmed the oligomerization state by gel filtration chromatography (Extended Data Fig. 1b), and investigated the impact of IRF3 activation and oligomerization status on p300s autoacetylation in the presence of a saturating concentration of $^{14}$C-labelled acetyl-CoA. p300s spans from the TAZ1 to the NCBD/IBiD domain and contains a deletion of the flexible N- and C-terminal regions (Fig. 1a). We found that p300s autoacetylated slowly in the absence of IRF3 (Extended Data Fig. 1c). Inclusion of inactive, monomeric IRF3 or IRF3ΔC did not significantly modify HAT activity (Fig. 1b and Extended Data Fig. 1c). In contrast, inclusion of active, TBK1-phosphorylated IRF3 dimers (pIRF3) resulted in a rapid burst of autoacetylation followed by a gradual increase of acetylated p300 (Fig. 1b). As IRF3ΔC did not support p300 HAT activation, we conclude that IRF3 dimerization and not merely p300 binding are essential for HAT activation.

p300 HAT activation was directly dependent on TBK1-mediated phosphorylation of IRF3 on Ser 396, a critical residue for IRF3 activation and dimerization[2,3]. Only when both TBK1 and IRF3 were included in the reaction did we observe phosphorylation of IRF3 on Ser 396 and p300 activation (Fig. 1d, Lane 4). We only observed a modest stimulatory effect of the adaptor protein STING (Fig. 1d, Lanes 7-12), likely due to the relatively high amounts of TBK1, which is already active and phosphorylates IRF3 even in the absence of STING[21]. Together, we conclude that IRF3 phosphorylation by TBK1 and its subsequent dimerization is required for p300 HAT activation.

To analyze the impact of pIRF3 on p300 activation and histone substrate acetylation, we established a scintillation proximity HAT assay (SPA), similar to that described previously[22]. We incubated saturating amounts of a biotinylated Histone H4 substrate peptide with p300s in the presence or absence of equimolar pIRF3 and increasing concentrations of [$^3$H] acetyl-CoA (Fig. 1e). As predicted, pIRF3 stimulated p300 histone substrate acetylation as determined by the increased rate of H4 acetylation obtained in the presence of pIRF3 ($V_{max}$ = 43.8 ± 5.3 cpm/min as compared to $V_{max}$ = 22.5 ± 2.8 cpm/min

106 in the absence of pIRF3). These data indicate that pIRF3 not only stimulates p300 autoacetylation and
107 activation, but also more efficient histone substrate acetylation.

108 We also investigated the effect of another well-known CBP/p300 ligand, STAT1, on p300 activation.
109 STATs are activated in response to cytokine receptor engagement and JAK kinase activation[23]. JAK-
110 mediated STAT1 phosphorylation on tyrosine 701 induces dimerization and translocation to the nucleus
111 where STAT1 binds to DNA elements to regulate gene expression. STAT1 contains a C-terminal
112 transactivation domain (TAD) through which it interacts with CBP/p300[7]. A naturally occurring splice
113 variant, STAT1β, lacks the TAD and acts in a dominant negative manner[24]. Structures of the active,
114 STAT1 Tyr701-phosphorylated dimer bound to DNA as well as the STAT1 TAD bound to the TAZ2
115 domain of CBP have been determined previously[25,26].

116 To understand the impact of STAT1 activation and oligomerisation status on p300 activity, we produced
117 STAT1ΔN lacking the N-domain (ND) and STAT1ΔNC lacking the ND and TAD as non-phosphorylated
118 monomers or as Tyr701-phosphorylated dimers (Extended Data Fig. 1e-h). We found that p300s
119 autoacetylated slowly in the absence of STAT1, and that addition of non-phosphorylated, monomeric
120 STAT1ΔN did not stimulate p300 autoacetylation beyond background levels (Fig. 1f, g). In contrast,
121 addition of Tyr701-phosphorylated STAT1ΔN (pSTAT1ΔN) dimers to p300s resulted in a rapid increase
122 of p300 autoacetylation. Activation required the C-terminal TAD of STAT1 as addition of a Tyr701-
123 phosphorylated STAT1 dimer (pSTAT1ΔNC), lacking the TAD, did not stimulate p300 autoacetylation
124 (Fig. 1f, g).

125 STAT1 dimerization, and not merely interaction with the TAZ2 domain, is required for activation of
126 p300. Unphosphorylated, monomeric STAT1ΔN, which contains the TAD and is able to interact with the
127 TAZ2 domain of CBP, did not stimulate p300 activity. Stimulation with STAT1 was however not as
128 potent as compared to that of IRF3, possibly because our STAT1 preparation is unphosphorylated on
129 Ser727, which is required for maximal gene activation[27,28]. Taken together, our data are in agreement with

a model in which the AIL peptide serves as an intramolecular 'pseudosubstrate' and competitive HAT inhibitor[19]. Dimeric ligands such as pIRF3 and pSTAT1 allow p300 activation by bringing two molecules together to enable trans-autoacetylation of the AIL, which in turn relieves autoinhibition and enables more efficient entry of histone substrates into the HAT active site.

**Structure of p300 adopts a AIL swap conformation**

To further understand the role of the AIL in regulation of these structural transitions, we crystallized the hypoacetylated form of BRP-HAT containing the AIL. Crystals were obtained using a similar protocol to that published previously[29]. Crystals diffracted to a minimal Bragg spacing of 3.1 A□ and we determined the structure by molecular replacement. The crystal form contained four p300 molecules in the asymmetric unit (Extended Data Table 1; Extended Data Fig. 2). Structural comparison with our previous structure (PDB; 4BHW) showed that the bromo-PHD-HAT domains overlay well on each other with a root–mean–square–deviation (RMSD) of ~ 1 A□. However the RING domains were not visible in the initial electron density map. Anomalous difference density maps showed a density peak for the zinc atom of the RING domain but not at the expected location. Manual repositioning allowed correct placement of the RING domains into the new position and refinement of the structure (Fig. 2a, Extended Data Fig. 3).

The p300 molecules show an antiparallel arrangement of the BRP-HAT domains (Extended Data Fig. 2a). In this configuration, the HAT domains from two neighboring molecules are closely apposed (Fig. 2a). In all protomers, AIL residues 1520–1532 adopt a helical extension of α6 which packs against the outwardly rotated RING domain of the neighboring protomer (Fig. 2a). In monomer II, residues 1566–1581 extend away from the HAT domain and associate with the substrate binding pocket of the HAT domain in monomer I, ~17 A□ away from the lysine substrate binding tunnel (Fig. 2B). The remainder of the AIL (residues 1532–1561) is disordered. In this conformation, positively charged residues K1568, K1569, K1570 project towards the highly electronegative substrate binding pocket of the HAT domain in

monomer I (Fig. 2c). As our SEC-MALLS shows that p300 is monomeric at low micromolar concentrations (see Extended Data Fig. 6), the AIL loop-swapped interactions do not appear to mediate formation of stable dimers, but may instead constitute more transient self-associations. Although the loop is clearly flexible and the electron density over the exchanged region not visible in all protomers (Fig. 2b, c, Extended Data Fig. 2b,c), this arrangement supports the interpretation that at high concentrations and when in close proximity to each other, two p300 monomers can engage each other by a AIL loop–swap.

**Structural rearrangement of the RING domain**

We previously proposed that active-site restriction by the RING domain is a negative regulatory mechanism for HAT activity[29]. A restricted active site is predicted to reduce the probability of substrates engaging with the active site by random diffusion and could thus be important in allowing for the regulation of acetylation by substrate recruitment. In agreement with this model, mutations that map to the structural framework that holds the RING domain in place result in HAT activation in cells[29]. In our current structure, the RING domain rotates by ~39° away from the HAT active site resulting in an overall displacement by ~22 Å as compared to the previously determined structure lacking the AIL (Fig. 3a). The axis of rotation is located perpendicular to the flexible loops L1 and L2 that connect the RING to the PHD domain.

The inward rotated conformation (magenta in Fig. 3a) is stabilized by interactions between Glu1242 of the RING domain and Arg1645 and Arg1646 of helix α9 of the HAT domain. In addition, Gln1173, Thr1174 and Thr1184 of the RING domain pack against the unusually long loop, L1 in the HAT domain that covers the CoA portion of the Lys-CoA inhibitor. As a result, Leu1182 resides within 5.5 Å of the lysine moiety of Lys–CoA (Fig. 3b). This inward conformation of the RING domain thus restricts substrate access to the HAT domain: The incoming AIL loop from the neighboring p300 monomer II would clash with the RING domain in the inward conformation (Fig. 3c).

In the outward rotated conformation, the interactions that attach the RING to the HAT domain are mostly disrupted (Fig. 3b). Leu1182 is positioned 15 Å away from the substrate-binding site and the RING domain is cradled by the AIL extension of helix α6 of the neighboring p300 molecule (monomer II residues 1524-1533; Fig. 3d). Despite shape complementarity, with a small buried surface area of ~320 $Å^2$ , the interface is predominantly polar, uncharacteristic of a typical protein-protein interface. However, the interaction could help to stabilize an outward rotated conformation of the RING domain and a more open HAT active site, apparently to enable AIL access and trans-acetylation.

**Regulation of HAT activity by flanking domains**

To systematically analyze the flanking domains, we generated a series of p300 constructs (Extended Data Fig. 4a) and analyzed the impact on HAT activity *in vitro* and in cells. Overexpression of p300 generally resulted in hyperacetylated, active p300 variants (Extended Data Fig. 4b,c) which likely masks the functional role of structural elements potentially involved in autoinhibition of deacetylated p300. Deletion of the RING domain did not drastically alter auto- or histone acetylation (Extended Data Fig. 5a). This deletion did not adversely affect structural integrity of p300, as shown by a crystal structure of the BRP module containing this deletion (Extended Data Fig. 5c).

Deletion of the AIL in all constructs resulted in decreased histone acetylation but bromodomain deletion (ΔBd) did not impact HAT function (Extended Data Fig. 5a, b). Together, we agree with previous observations made for CBP that at least in the active, hyperacetylated state of the enzyme, RING deletion does not substantially impact HAT activity and that the p300 AIL positively contributes to substrate acetylation[30]. We next introduced mutations into full-length p300 and monitored their effect on p300 auto- and p53 acetylation upon transient co-overexpression in cells. Deletion of the RING and CH3 domains resulted in significantly increased p300 and p53 acetylation but deletion of the Bd or AIL had no major impact (Extended Data Fig. 5e). As expected, introduction of the catalytic mutants D1399Y or

Y1467F abolished p300 or p53 acetylation (Extended Data Fig. 5e). Immunofluorescence analysis showed that wild-type p300 as well as a ΔBd and ΔAIL deletion were uniformly distributed in the nucleus but that the HAT activating p300 variants ΔRING and ΔCH3, formed nuclear foci that co-localized with p53 (Extended Data Fig. 5d). To validate these results, we analyzed and confirmed the phenotype of p300 mutants and p53 acetylation in another cell line (Fig. 4a, b). In addition, we analyzed p300 variants in which eleven lysine amino acids of the AIL segment K1546-1570 were mutated to arginine or glutamate and found reduced or slightly increased p300 autoacetylation or p53 levels, respectively (Fig. 4a, b).

As we observed formation of nuclear foci only with HAT activating variants, we hypothesized that hyperacetylation drives p300 to form biomolecular condensates in cells. Accordingly, introduction of a HAT inactivating D1399Y mutation into p300 ΔRING, treatment with the p300 HAT inhibitor A-485[22] or with the CBP/p300 Bd inhibitor CBP30 greatly reduced foci formation (Fig. 4c). We therefore conclude that HAT activation drives biomolecular condensation of p300 in cells apparently through Bd substrate engagement.

**AIL acetylation and RING domain repositioning regulate a dynamic interaction with the p300 substrate binding pocket**

We next sought to understand how the highly conserved and intrinsically disordered AIL segment contributes to regulation of the catalytic function of p300. The AIL spanning amino acid residues 1532-1567 is positively charged in the deacetylated state, with an estimated isoelectric point (pI) of 10.9, and net charge of 7 at neutral pH. In contrast, upon autoacetylation of residues spanning Lys1542-1560[31], we estimate a pI of 3.5 and a net charge of –2. As the proximal substrate binding groove of p300 is largely acidic (Fig. 3c), we hypothesized, in agreement with earlier predictions[32], that a deacetylated AIL would engage the substrate binding site through electrostatic interactions, presumably to prevent access of

positively charged lysine-containing substrates. Given the disordered nature of the AIL, this proposed interaction is expected to be highly dynamic[30].

We tested this postulate through all-atom Monte Carlo simulations[33]. To make this approach tractable, our simulations held the backbone dihedral angles associated with the folded domains fixed, but all other degrees of freedom, including all backbone and sidechain dihedral angles in the AIL were fully sampled. As a result, these simulations should be seen as assessing how the AIL interacts with the remainder of p300 given the observed crystal structure. Simulations were performed on the AIL in the deacetylated and acetylated state in the context of the p300 monomer. These simulations allowed us to interrogate how acetylation influenced the conformation and intra-molecular interactions of the AIL.

Simulations of the deacetylated AIL revealed the presence of extensive yet highly degenerate electrostatic interactions between the AIL and the RING domain and HAT substrate binding site. These interactions were quantifiable in terms of the normalized distances between pairs of amino acid residues (Fig. 5a and movie Extended Data Fig. 5). Lysine residues in the AIL dynamically associate through long-range electrostatic interactions with acidic residues (E1334, E1442, E1505, D1622, D1625 and D1628) in the p300 HAT substrate binding pocket (Fig. 5c). The importance of these residues for substrate acetylation has been shown previously[34], and NMR data for CBP confirm that the AIL is intrinsically disordered in the deacetylated state[30].

In contrast, in the acetylated state, we found no interactions between the AIL and the substrate binding site (Fig. 5b and movie Extended Data Fig. 5). The acetylated AIL essentially behaved like a self-avoiding random coil without any strong biases for interaction with itself or with the surrounding folded domains, including the Bd. It has been proposed that the AIL of CBP, when acetylated on K1596 (K1558 in p300), engages the Bd intramolecularly thus competing with histone binding and negatively regulating substrate acetylation [30]. Isothermal calorimetry experiments showed highest binding affinity for multiacetylated peptides including diacetylated histone H3 K14acK18ac or H4 K12acK16ac peptides,

generally following the pattern KacNNNKac (Extended Data Table 2). Monoacetylated peptides typically had weaker binding affinity. A crystal structure of the H4 K12acK16ac peptide bound to BPΔR (Extended Data Fig. 5c) confirmed the acetyllysine-specific binding mode. However, a AIL peptide acetylated on three lysines K1549, K1558, K1560, corresponding to some of the most highly acetylated residues in the AIL[31], failed to bind to the BRP module. Thus our model is that the multiacetylated AIL is not a substrate for the Bd, presumably because of suboptimal spacing or sequence environment of the AIL Kac sites.

To understand how the RING domain influences the ability of substrates, including the AIL, to enter the active site of an adjacent p300 molecule, we performed simulations of the AIL in context of the loop-swapped dimer with a harmonic potential to maintain the AIL in the active site to assess potential inter-molecular interactions (Fig. 5d, e). In the active RING conformation, the AIL is able to engage the substrate binding site. However, in the inactive conformation, the frequency of contacts between the AIL and the acidic active site residues E1442 and D1444, residues proximal to the lysine substrate binding tunnel, was reduced by 70-75% (Fig. 5d). These results suggest that in the inactive conformation the RING domain at least partially reduces catalytic activity by limiting accessibility of the active site to the AIL and other substrates.

One prediction from our models is that the deacetylated form of p300 adopts a more compact conformation, due to dynamic engagement of the AIL with the HAT substrate-binding site, while the acetylated form adopts a more 'open' conformation (Fig. 5d). To test this possibility, we produced deacetylated p300 variants by treatment with SIRT2 as shown previously[29], and hyperacetylated forms by acetylation with the p300 HAT domain. Mass spectroscopy showed that this procedure allowed us to obtain hypo- or hyperacetylated p300 variants (Extended Data Fig. 6d-f).

We analyzed these preparations by multi-angle laser light scattering coupled to size exclusion chromatography (SEC-MALLS). All preparations, irrespective of the acetylation status, were monomeric at the concentration tested (2 $mg \cdot ml^{-1}$) (Extended Data Fig. 6a-c, Table 1). Comparison of hypo- and

hyperacetylated p300 BRP-HAT showed a small decrease in the elution volume indicative of a larger hydrodynamic radius upon hyperacetylation (Extended Data Fig. 6a). A similar result was obtained upon comparison of hyper- and hypoacetylated BRP-HAT-CH3 (Extended Data Fig. 6b). In contrast, a variant lacking the AIL showed no shift in the elution volume upon hyperacetylation (Extended Data Fig. 6b). Thus our data agree with the model that the catalytic p300 'core' spanning the BRP-HAT-CH3 domains, adopts a compact conformation in the hypoacetylated state and that autoacetylation results in a more extended conformation.

## Discussion

Our findings represent, to our knowledge, the first detailed mechanistic insights into how cellular signaling controls activity of a chromatin regulator. We propose a multi-step process for p300 HAT activation and signal transmission to chromatin (Fig. 6). First, in the basal state, the deacetylated AIL is expected to maintain an overall positively charged environment in close proximity to the enzyme's active site, which prevents access of positively charged lysine-rich substrates. Direct access to the CoA binding tunnel and autoacetylation of the AIL *in cis* appears to be prohibited, in part due to positioning of the RING domain (Fig. 5d). The interaction between the AIL and the HAT substrate binding pocket is reminiscent of polyelectrostatic binding, in which specificity and affinity are achieved without the acquisition of structure[35]. Electrostatically-mediated interactions driven by high densities of lysine residues have recently been shown to engender extremely high affinity binding[36]. Our results are at least consistent with a model in which the AIL strongly interacts with the active site in an inhibitory fashion through a combination of lysine multivalency coupled with a high local concentration mediated by the position of the AIL. However, this model does not rule out the possibility that certain lysine residues may be more important for inhibition than others.

296 Cellular signaling initiates phosphorylation of TFs, such as IRF3 or STAT1, which results in their
297 activation and dimerization. The activated dimeric TFs are in their DNA-binding competent conformation
298 and can engage two copies of p300 in the nucleus. The likelihood of AIL disengagement from its
299 inhibitory position *in cis* and capture *in trans* by a second p300 copy is increased when p300 is bound to
300 activated dimeric TFs. Transient association of two p300 copies does not necessarily require precise
301 stereospecific interactions between the structured domains as acetylation at multiple lysines in the AIL
302 indicates a series of possible conformations in such associating dimers. We predict that regulated
303 oligomerisation uncouples recruitment from HAT activation which could explain why not all CBP/p300
304 recruitment events result in chromatin acetylation and gene activation[13-18,37].

305 It has been recently proposed that enhancer RNA (eRNA) interacts with the AIL to regulate CBP HAT
306 activity[38]. We have attempted to reproduce these results using Klf6, one of the most potent eRNAs
307 reported[38]. We could not detect p300 HAT activation using up to equimolar amounts of Klf6 (Extended
308 Data Fig. 7a). We note that Bose et al. purify CBP in buffer containing EDTA, which is detrimental to the
309 structure of CBP/p300 due to the presence of multiple zinc-binding domains[39]. Unfolded CBP/p300 have
310 a high tendency to aggregate, and to form non-specific interactions[39]. Paradoxically, as the HAT domain
311 is not affected, inclusion of EDTA can have an 'activating' effect in biochemical assays, apparently due
312 to such non-specific aggregation (Extended Data Fig. 7b). The detrimental effects of EDTA on the
313 structure and function of CBP/p300 need to be taken into account in the interpretation of such data.

314 The ability of certain histone-modifying enzymes to bind to the PTM they generate has led to models
315 where such enzymes might propagate modified chromatin domains by a positive-feedback loop[40].
316 According to this view histone PTMs and other chromatin modifications form an additional, DNA
317 sequence-independent layer of the genome which is read out by enzymes that recognize these
318 modifications to 'epigenetically' regulate genomic function[40]. An alternative view posits that histone
319 PTMs ultimately depend on DNA sequence-dependent recruitment of chromatin modifiers and so do not
320 necessarily form an independent 'epigenetic' layer of the genome[8,41-43]. The controversy has arisen

because it has been difficult to disentangle, for most chromatin regulators, the relative contributions of DNA targeting and histone PTM substrate engagement to the overall chromatin modification reaction.

We show here that regulation of the p300 HAT activity is intricately linked to the activation and oligomerisation status of TF ligands and we therefore conclude that specificity for p300-mediated chromatin targeting and acetylation arises mainly through TF-mediated and DNA sequence-dependent genome targeting. How then does the BRP 'PTM reader' module contribute to p300 function? So far it has been difficult to determine its precise contribution: While it is clear that the Bd can engage acetylated histone peptides and bind to hyperacetylated chromatin[29,44,45], deletion or mutation of the Bd has no apparent effect on substrate acetylation[29,46], has only minimal effects in a hematopoiesis model system[47], and Bd inhibition does not adversely affect genome targeting of CBP[48].

We favor the view that DNA binding provides the lead anchoring mechanism and that Bd substrate engagement contributes to signal maintenance: Local hyperacetylation increases the binding valency by allowing Bd substrate engagement, which further helps to compartmentalize the biochemical reaction and to contribute to signal maintenance through positive feedback[45]. Accordingly, p300 HAT activating mutants form biomolecular condensates in cells when transiently overexpressed (Fig. 4c, Extended Data Fig. 5d). Treatment with a HAT or Bd inhibitor greatly reduces condensate formation, indicating that hyperacetylation is critical in driving assembly, apparently due to increased binding valency involving Bd-substrate engagement. The formation of condensates, possibly through phase-separation, may provide a mechanism to enable signal integration on enhancers and transcriptional control as suggested previously[49]. We note that establishment and long-term maintenance of silenced chromatin by methyltransferases such as Suv39/Clr4 and PRC2 requires DNA sequence-specific recruitment and also does not seem to occur independently of DNA targeting[50-52]. It will be critical to disentangle cause-effect relationships of DNA targeting, chromatin modification and histone PTM substrate engagement of other chromatin regulators.

**Data availability.** Coordinates for the p300 core structure and BPΔR bound to a diacetylated histone H4 peptide are available from the Protein Data Bank under accession number XXX and XXX, respectively.


## Acknowledgements

This work was in part supported by a grant from the Worldwide Cancer Research charity. EO was supported by an EMBL Interdisciplinary Postdoctoral (EIPOD) fellowship. SR was supported by a postdoctoral fellowship from the Fondation ARC pour la recherche sur le Cancer and has received support from the Fondation FINOVI. ASH is a postdoctoral fellow in the laboratory of Dr. Rohit V. Pappu (RVP) at Washington University in St. Louis. The computational contributions to this work were supported in, in part, by the Human Frontiers Science Program (grant RGP0034/2017 to RVP) and the St. Jude Collaborative Research Consortium on Membraneless Organelles (to RVP). We thank the staff at the ESRF beamlines BM29, ID30a–1,3 (MASSIF) for their support during data collection. We thank Joanna Kirkpatrick and the proteomic core facility at EMBL for processing and analysis of samples. We thank the Partnership for Structural Biology (Grenoble) for providing access to their biophysical platform. We thank Russel Vance (University of California, Berkeley, CA) for the plasmid encoding GST-STING. We thank Philip A. Cole (Harvard Medical School) for the A-485 inhibitor. SK laboratory is supported by ANR Episperm3 program. Additional support was from: Fondation ARC "Canc'air" project (RAC16042CLA), Plan Cancer (CH7-INS15B66) and Plan Cancer (ASC16012CSA) and the "Université Grenoble Alpes" ANR-15-IDEX-02 LIFE and IDEX SYMER.


## *Author contributions*

E.O, Z.I, S.R., N.H, and J.G. performed the experiments. A.S.H. performed structural modeling. E.O, S.R., S. K. and D. P. designed experiments and analyzed data. D.P. wrote the manuscript. All authors commented on the manuscript.

## References


1 Chen, Q., Sun, L. & Chen, Z. J. Regulation and function of the cGAS-STING pathway of cytosolic DNA sensing. *Nature immunology* **17**, 1142-1149, doi:10.1038/ni.3558 (2016).

2 Panne, D., McWhirter, S. M., Maniatis, T. & Harrison, S. C. Interferon regulatory factor 3 is regulated by a dual phosphorylation-dependent switch. *J. Biol. Chem.* **282**, 22816-22822, doi:M703019200 [pii]

10.1074/jbc.M703019200 (2007).

3 Zhao, B. *et al.* Structural basis for concerted recruitment and activation of IRF-3 by innate immune adaptor proteins. *Proc. Natl. Acad. Sci. U. S. A.* **113**, E3403-3412, doi:10.1073/pnas.1603269113 (2016).

4 Parekh, B. S. & Maniatis, T. Virus infection leads to localized hyperacetylation of histones H3 and H4 at the IFN-beta promoter. *Mol. Cell* **3**, 125-129 (1999).

5 Panne, D., Maniatis, T. & Harrison, S. C. An atomic model of the interferon-beta enhanceosome. *Cell* **129**, 1111-1123, doi:S0092-8674(07)00656-3 [pii]

10.1016/j.cell.2007.05.019 (2007).

6 Stark, G. R. & Darnell, J. E., Jr. The JAK-STAT pathway at twenty. *Immunity* **36**, 503-514, doi:10.1016/j.immuni.2012.03.013 (2012).

7 Zhang, J. J. *et al.* Two contact regions between Stat1 and CBP/p300 in interferon gamma signaling. *Proc. Natl. Acad. Sci. U. S. A.* **93**, 15092-15096 (1996).

8 Bedford, D. C. & Brindle, P. K. Is histone acetylation the most important physiological function for CBP and p300? *Aging (Albany NY)* **4**, 247-255 (2012).

9 Heintzman, N. D. *et al.* Distinct and predictive chromatin signatures of transcriptional promoters and enhancers in the human genome. *Nat. Genet.* **39**, 311-318, doi:ng1966 [pii]

10.1038/ng1966 (2007).

10 Visel, A. *et al.* ChIP-seq accurately predicts tissue-specific activity of enhancers. *Nature* **457**, 854-858, doi:nature07730 [pii]

10.1038/nature07730 (2009).

11 Creyghton, M. P. *et al.* Histone H3K27ac separates active from poised enhancers and predicts developmental state. *Proc. Natl. Acad. Sci. U. S. A.* **107**, 21931-21936, doi:10.1073/pnas.1016071107 (2010).

12 Jin, Q. *et al.* Distinct roles of GCN5/PCAF-mediated H3K9ac and CBP/p300-mediated H3K18/27ac in nuclear receptor transactivation. *EMBO J.* **30**, 249-262, doi:10.1038/emboj.2010.318 (2011).

13 Bedford, D. C., Kasper, L. H., Fukuyama, T. & Brindle, P. K. Target gene context influences the transcriptional requirement for the KAT3 family of CBP and p300 histone acetyltransferases. *Epigenetics : official journal of the DNA Methylation Society* **5**, 9-15 (2010).

14 Zhao, L. *et al.* Integrated genome-wide chromatin occupancy and expression analyses identify key myeloid pro-differentiation transcription factors repressed by Myb. *Nucleic Acids Res.* **39**, 4664-4679, doi:10.1093/nar/gkr024 (2011).

15 Waltzer, L. & Bienz, M. Drosophila CBP represses the transcription factor TCF to antagonize Wingless signalling. *Nature* **395**, 521-525, doi:10.1038/26785 (1998).

16 Holmqvist, P. H. & Mannervik, M. Genomic occupancy of the transcriptional co-activators p300 and CBP. *Transcription* **4**, 18-23, doi:10.4161/trns.22601 (2013).

17 Kasper, L. H., Qu, C., Obenauer, J. C., McGoldrick, D. J. & Brindle, P. K. Genome-wide and single-cell analyses reveal a context dependent relationship between CBP recruitment and gene expression. *Nucleic Acids Res.* **42**, 11363-11382, doi:10.1093/nar/gku827 (2014).

18 Rada-Iglesias, A. *et al.* A unique chromatin signature uncovers early developmental enhancers in humans. *Nature*, doi:nature09692 [pii]

10.1038/nature09692 (2010).

19 Thompson, P. R. *et al.* Regulation of the p300 HAT domain via a novel activation loop. *Nat. Struct. Mol. Biol.* **11**, 308-315, doi:10.1038/nsmb740

nsmb740 [pii] (2004).

20 Qin, B. Y. *et al.* Crystal structure of IRF-3 in complex with CBP. *Structure* **13**, 1269-1277 (2005).

21 Larabi, A. *et al.* Crystal structure and mechanism of activation of TANK-binding kinase 1. *Cell reports* **3**, 734-746, doi:10.1016/j.celrep.2013.01.034 (2013).

22 Lasko, L. M. *et al.* Discovery of a selective catalytic p300/CBP inhibitor that targets lineage-specific tumours. *Nature* **550**, 128-132, doi:10.1038/nature24028 (2017).

23 Levy, D. E. & Darnell, J. E., Jr. Stats: transcriptional control and biological impact. *Nat. Rev. Mol. Cell Biol.* **3**, 651-662, doi:10.1038/nrm909 (2002).

24 Shuai, K., Stark, G. R., Kerr, I. M. & Darnell, J. E., Jr. A single phosphotyrosine residue of Stat91 required for gene activation by interferon-gamma. *Science* **261**, 1744-1746 (1993).

25 Chen, X. *et al.* Crystal structure of a tyrosine phosphorylated STAT-1 dimer bound to DNA. *Cell* **93**, 827-839, doi:S0092-8674(00)81443-9 [pii] (1998).

26 Wojciak, J. M., Martinez-Yamout, M. A., Dyson, H. J. & Wright, P. E. Structural basis for recruitment of CBP/p300 coactivators by STAT1 and STAT2 transactivation domains. *EMBO J.* **28**, 948-958, doi:emboj200930 [pii]

10.1038/emboj.2009.30 (2009).

27 Darnell, J. E., Jr. STATs and gene regulation. *Science* **277**, 1630-1635 (1997).

28 Ramsauer, K. *et al.* Distinct modes of action applied by transcription factors STAT1 and IRF1 to initiate transcription of the IFN-gamma-inducible gbp2 gene. *Proc. Natl. Acad. Sci. U. S. A.* **104**, 2849-2854, doi:10.1073/pnas.0610944104 (2007).

29 Delvecchio, M., Gaucher, J., Aguilar-Guerreri, C., Ortega, E. & Panne, D. Structure of the p300 catalytic core and implications for chromatin targeting and HAT regulation. *Nat. Struct. Mol. Biol.* **21**, doi:10.1038/nsmb.2642 (2013).

30 Park, S. *et al.* Role of the CBP catalytic core in intramolecular SUMOylation and control of histone H3 acetylation. *Proc. Natl. Acad. Sci. U. S. A.* **114**, E5335-E5342, doi:10.1073/pnas.1703105114 (2017).

31 Karanam, B., Jiang, L., Wang, L., Kelleher, N. L. & Cole, P. A. Kinetic and mass spectrometric analysis of p300 histone acetyltransferase domain autoacetylation. *J. Biol. Chem.* **281**, 40292-40301, doi:10.1074/jbc.M608813200 (2006).

32 Karanam, B. *et al.* Multiple roles for acetylation in the interaction of p300 HAT with ATF-2. *Biochemistry (Mosc).* **46**, 8207-8216, doi:10.1021/bi7000054 (2007).

33 Vitalis, A. & Pappu, R. V. ABSINTH: a new continuum solvation model for simulations of polypeptides in aqueous solutions. *Journal of computational chemistry* **30**, 673-699, doi:10.1002/jcc.21005 (2009).

34 Liu, X. *et al.* The structural basis of protein acetylation by the p300/CBP transcriptional coactivator. *Nature* **451**, 846-850, doi:nature06546 [pii]

10.1038/nature06546 (2008).

35 Borg, M. *et al.* Polyelectrostatic interactions of disordered ligands suggest a physical basis for ultrasensitivity. *Proc. Natl. Acad. Sci. U. S. A.* **104**, 9650-9655, doi:10.1073/pnas.0702580104 (2007).

36 Borgia, A. *et al.* Extreme disorder in an ultrahigh-affinity protein complex. *Nature*, doi:10.1038/nature25762 (2018).

37 Soutoglou, E. *et al.* Transcription factor-dependent regulation of CBP and P/CAF histone acetyltransferase activity. *EMBO J.* **20**, 1984-1992, doi:10.1093/emboj/20.8.1984 (2001).

38 Bose, D. A. *et al.* RNA Binding to CBP Stimulates Histone Acetylation and Transcription. *Cell* **168**, 135-149 e122, doi:10.1016/j.cell.2016.12.020 (2017).

39 Matt, T., Martinez-Yamout, M. A., Dyson, H. J. & Wright, P. E. The CBP/p300 TAZ1 domain in its native state is not a binding partner of MDM2. *Biochem. J.* **381**, 685-691, doi:10.1042/BJ20040564 (2004).

40 Allis, C. D. & Jenuwein, T. The molecular hallmarks of epigenetic control. *Nature reviews. Genetics* **17**, 487-500, doi:10.1038/nrg.2016.59 (2016).

41 Ptashne, M. Epigenetics: core misconcept. *Proc. Natl. Acad. Sci. U. S. A.* **110**, 7101-7103, doi:10.1073/pnas.1305399110 (2013).

42 Rando, O. J. Combinatorial complexity in chromatin structure and function: revisiting the histone code. *Curr. Opin. Genet. Dev.* **22**, 148-155, doi:10.1016/j.gde.2012.02.013 (2012).

43 Henikoff, S. & Shilatifard, A. Histone modification: cause or cog? *Trends Genet.* **27**, 389-396, doi:10.1016/j.tig.2011.06.006 (2011).

44 Filippakopoulos, P. *et al.* Histone recognition and large-scale structural analysis of the human bromodomain family. *Cell* **149**, 214-231, doi:10.1016/j.cell.2012.02.013 (2012).

45 Nguyen, U. T. *et al.* Accelerated chromatin biochemistry using DNA-barcoded nucleosome libraries. *Nature methods* **11**, 834-840, doi:10.1038/nmeth.3022 (2014).

46 Rack, J. G. *et al.* The PHD finger of p300 Influences Its Ability to Acetylate Histone and Non-Histone Targets. *J. Mol. Biol.*, doi:10.1016/j.jmb.2014.08.011 (2014).

47 Kimbrel, E. A. *et al.* Systematic in vivo structure-function analysis of p300 in hematopoiesis. *Blood* **114**, 4804-4812, doi:10.1182/blood-2009-04-217794 (2009).

48 Picaud, S. *et al.* Generation of a Selective Small Molecule Inhibitor of the CBP/p300 Bromodomain for Leukemia Therapy. *Cancer Res.* **75**, 5106-5119, doi:10.1158/0008-5472.CAN-15-0236 (2015).

49 Hnisz, D., Shrinivas, K., Young, R. A., Chakraborty, A. K. & Sharp, P. A. A Phase Separation Model for Transcriptional Control. *Cell* **169**, 13-23, doi:10.1016/j.cell.2017.02.007 (2017).

50 Coleman, R. T. & Struhl, G. Causal role for inheritance of H3K27me3 in maintaining the OFF state of a Drosophila HOX gene. *Science* **356**, doi:10.1126/science.aai8236 (2017).

51 Laprell, F., Finkl, K. & Muller, J. Propagation of Polycomb-repressed chromatin requires sequence-specific recruitment to DNA. *Science* **356**, 85-88, doi:10.1126/science.aai8266 (2017).

52 Wang, X. & Moazed, D. DNA sequence-dependent epigenetic inheritance of gene silencing and histone H3K9 methylation. *Science* **356**, 88-91, doi:10.1126/science.aaj2114 (2017).

53 Crooks, G. E., Hon, G., Chandonia, J. M. & Brenner, S. E. WebLogo: a sequence logo generator. *Genome Res.* **14**, 1188-1190, doi:10.1101/gr.849004 (2004).

54 Luger, K., Rechsteiner, T. J. & Richmond, T. J. Preparation of nucleosome core particle from recombinant histones. *Methods Enzymol.* **304**, 3-19, doi:S0076-6879(99)04003-3 [pii] (1999).

55 McGibbon, R. T. *et al.* MDTraj: A Modern Open Library for the Analysis of Molecular Dynamics Trajectories. *Biophys. J.* **109**, 1528-1532, doi:10.1016/j.bpj.2015.08.015 (2015).

56 Holehouse, A. S., Garai, K., Lyle, N., Vitalis, A. & Pappu, R. V. Quantitative assessments of the distinct contributions of polypeptide backbone amides versus side chain groups to chain expansion via chemical denaturation. *J. Am. Chem. Soc.* **137**, 2984-2995, doi:10.1021/ja512062h (2015).

57 Schneider, C. A., Rasband, W. S. & Eliceiri, K. W. NIH Image to ImageJ: 25 years of image analysis. *Nature methods* **9**, 671-675 (2012).

58 Kaczmarska, Z. *et al.* Structure of p300 in complex with acyl-CoA variants. *Nature chemical biology* **13**, 21-29, doi:10.1038/nchembio.2217 (2017).

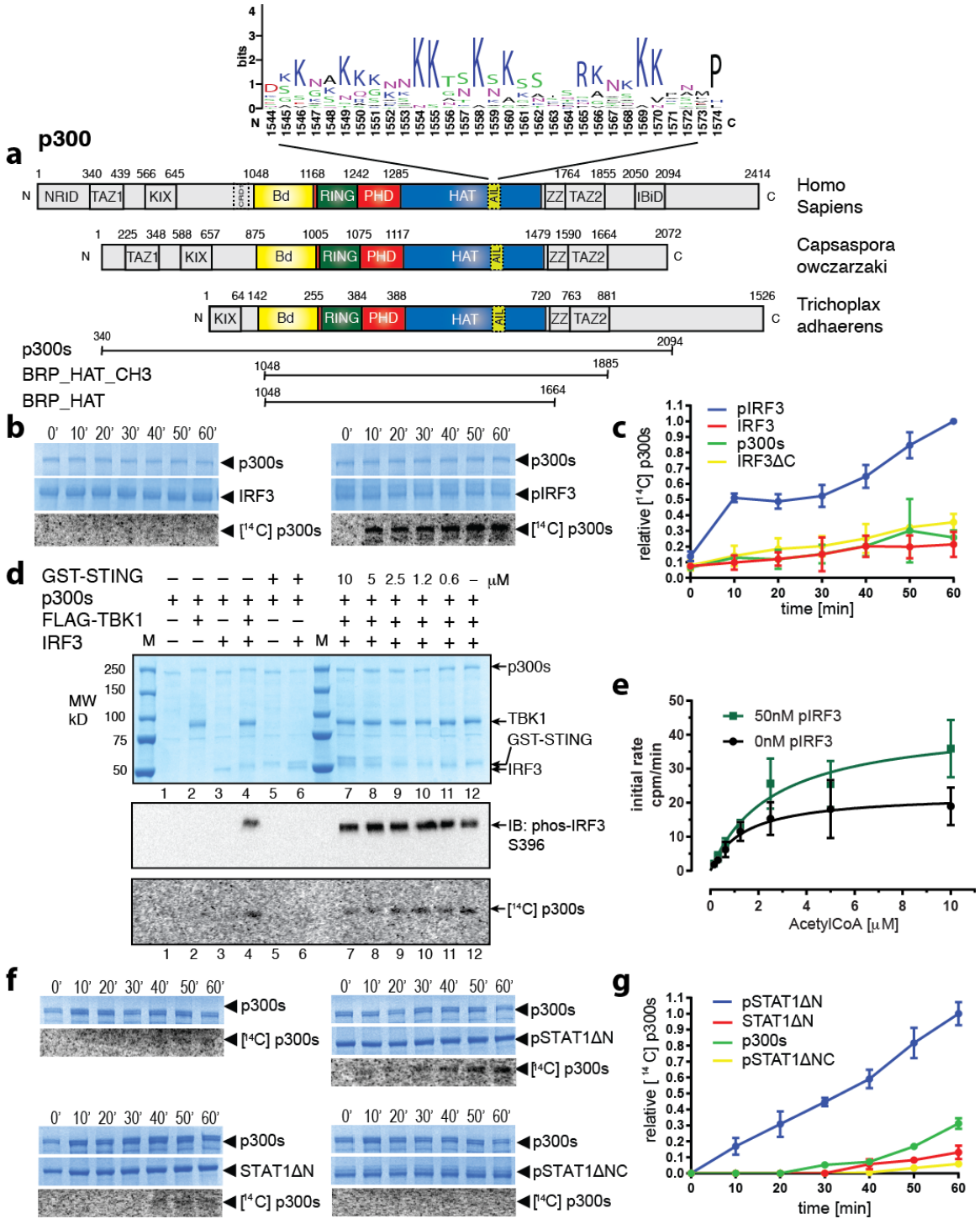


**Figure 1. Transcription factor dimerization enables activation of p300. (a)** Domain structure of p300. Sequence conservation of the AIL is shown using WebLogo[53]. Constructs used are shown. **(b)** p300s was incubated for the indicated times in the presence or absence of inactive, monomeric IRF3 or TBK1-phosphorylated, dimeric pIRF3. Samples were analyzed by SDS-PAGE followed by Coomassie staining and autoradiography. (**c**) Quantification of autoacetylation of p300s. (**d**) p300 is activated by TBK1-mediated IRF3 phosphorylation. p300s was incubated with recombinant GST-STING, TBK1 and IRF3 in

the presence of ATP and [$^{14}$C] acetyl-CoA. Top panel: Coomassie-stained SDS-PAGE gel. Middle panel: Analysis of IRF3 phosphorylation on S396 using immunoblotting. Bottom panel: autoradiography. (**e**) HAT scintillation proximity assay. 12.5 μM Histone H4 substrate peptide was incubated with 50 nM p300s in the presence (green) or absence (black) of 50 nM pIRF3 and varying concentrations of [$^{3}$H] acetyl-CoA. The degree of Histone H4 substrate acetylation was quantified using scintillation counting. (**f**) As in panel B but using inactive, monomeric STAT1ΔN or activated, dimeric pSTAT1ΔN. Activated, dimeric pSTAT1ΔNC lacking the C-terminal TAD did not stimulate p300s autoacetylation. Samples were analyzed as in panel (B). (**g**) Quantification of autoacetylation of p300s. Intensity values were normalized by dividing by the maximum autoacetylation signal obtained after 60 minutes. Error bars shown in panels (**c**), (**e**) and (**g**): Three independent experiments were performed and the mean value and error bars representing the standard deviation are shown. Data analysis and plotting was done with Graphpad Prism 7.0.

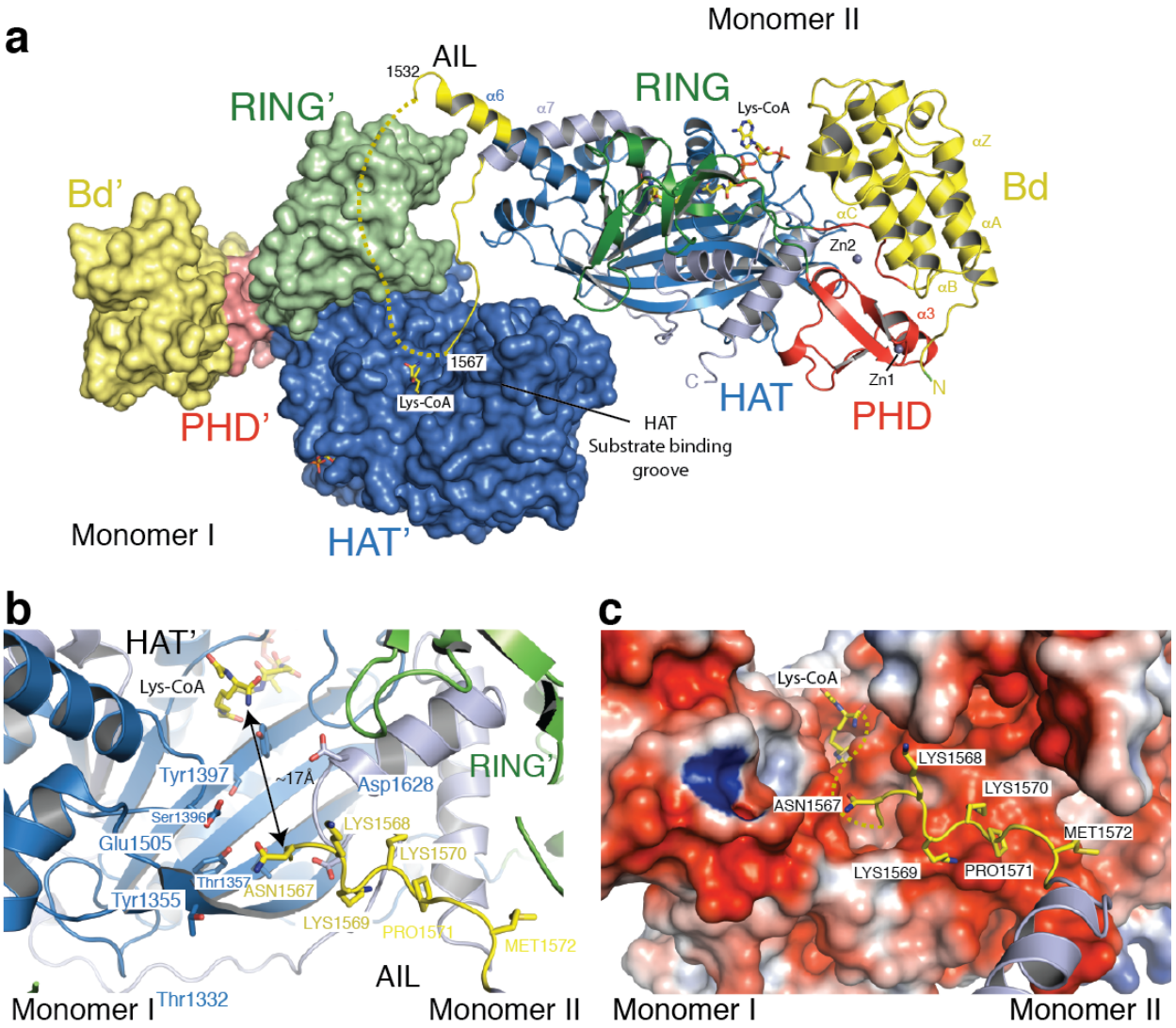


**Figure 2: The structure of p300 adopts a AIL swap conformation. (a)** Monomer I is surface rendered and monomer II is shown as a cartoon. The AIL loop from monomer II is shown in yellow. The AIL lies near the HAT substrate binding groove of monomer I. A disordered segment of the AIL is shown as a dotted line. **(b)** Close up view of the residues of the AIL loop from monomer II and residues of monomer I in the substrate binding pocket. **(c)** Binding of the positively charged AIL is mediated by interactions with negatively charged residues in the HAT binding pocket.

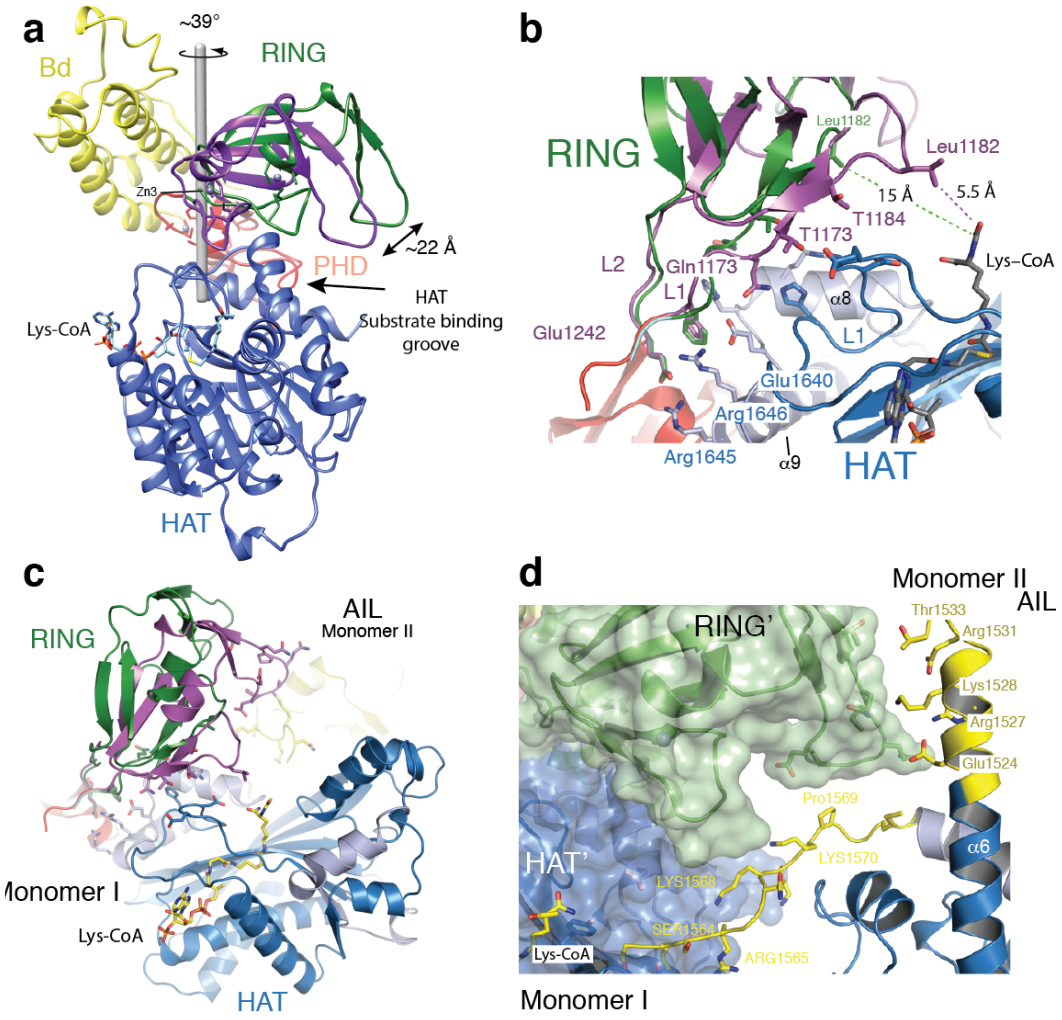


544

545 **Figure 3: Structural rearrangement of the RING domain. (a)** The RING domain (green) rotates ~39°
546 resulting in a 22 Å displacement away from the active site. The rotation axis is indicated as a grey rod. **(b)**
547 In the loop-swap conformation, residues in the RING-HAT interface are disrupted thus resulting in a
548 more open HAT active site. Leu1182 is positioned 15Å away from the Lys-CoA inhibitor in the loop-
549 swap conformation (green) but within 5.5Å in the absence of the loop swap (magenta). **(c)** Repositioning
550 of the RING domain allows the AIL from monomer II to approach the HAT active site of monomer I. **(d)**
551 Details of the interaction surface of the AIL from monomer II with the RING domain of monomer I.

552

553

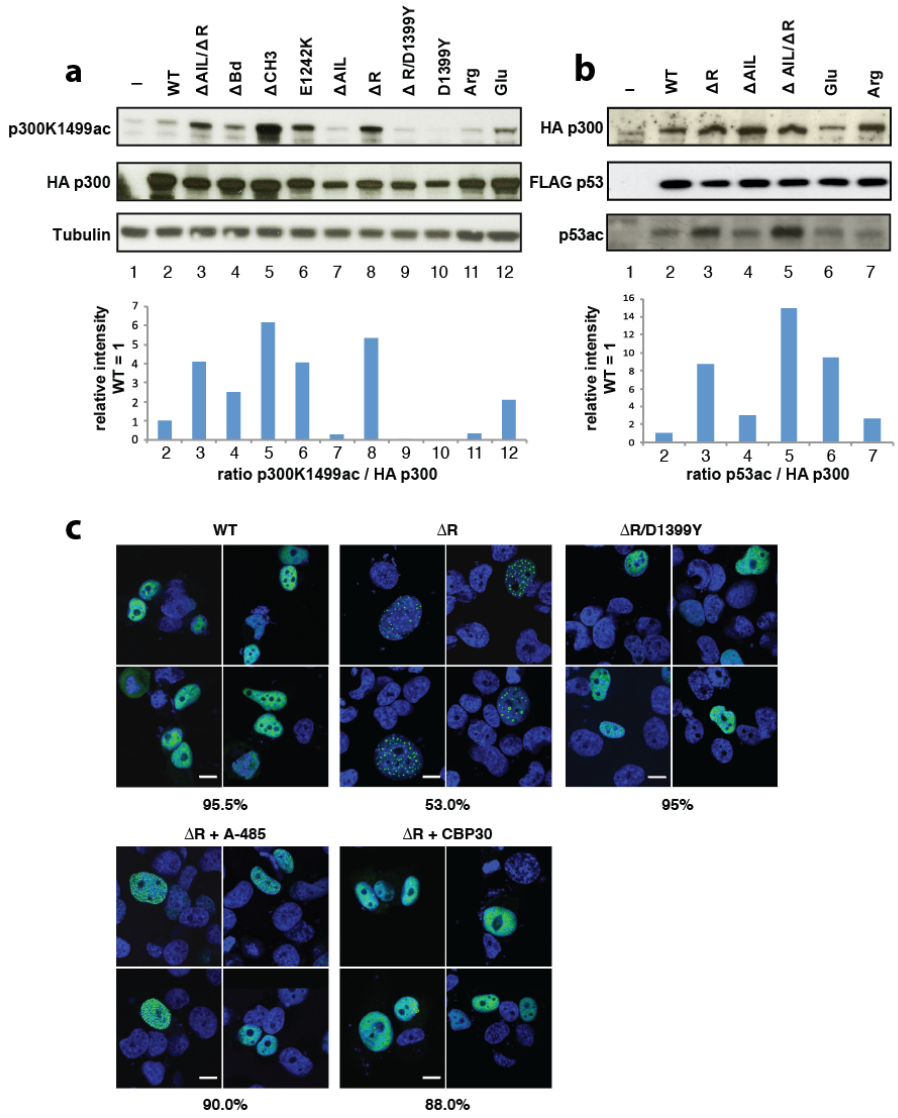


554

555

556 **Figure 4: Regulation of HAT activity by flanking domains.** (**a**) Indicated variants of p300 were
557 transiently co-transfected with p53 in COS cells and samples analyzed by western blotting using the
558 indicated antibodies. Bottom panel: quantification p300 K1499Ac signal. (**b**) Analysis of p53 acetylation.
559 Bottom panel: quantification p53 acetylation signal. (**c**) H1299 cells were transfected with the indicated
560 construct and analyzed by immunoflorescence using Anti-HA for p300 (green) and cell nuclei were
561 stained with Hoechst (blue). Bottom panels: Cells were treated with the A-485 HAT or the CBP30
562 Bromodomain inhibitor. Percentage of cells showing the indicated phenotype (n=200 cells) is indicated
563 below each panel. Scale bar, 10 µm.

564

565

566

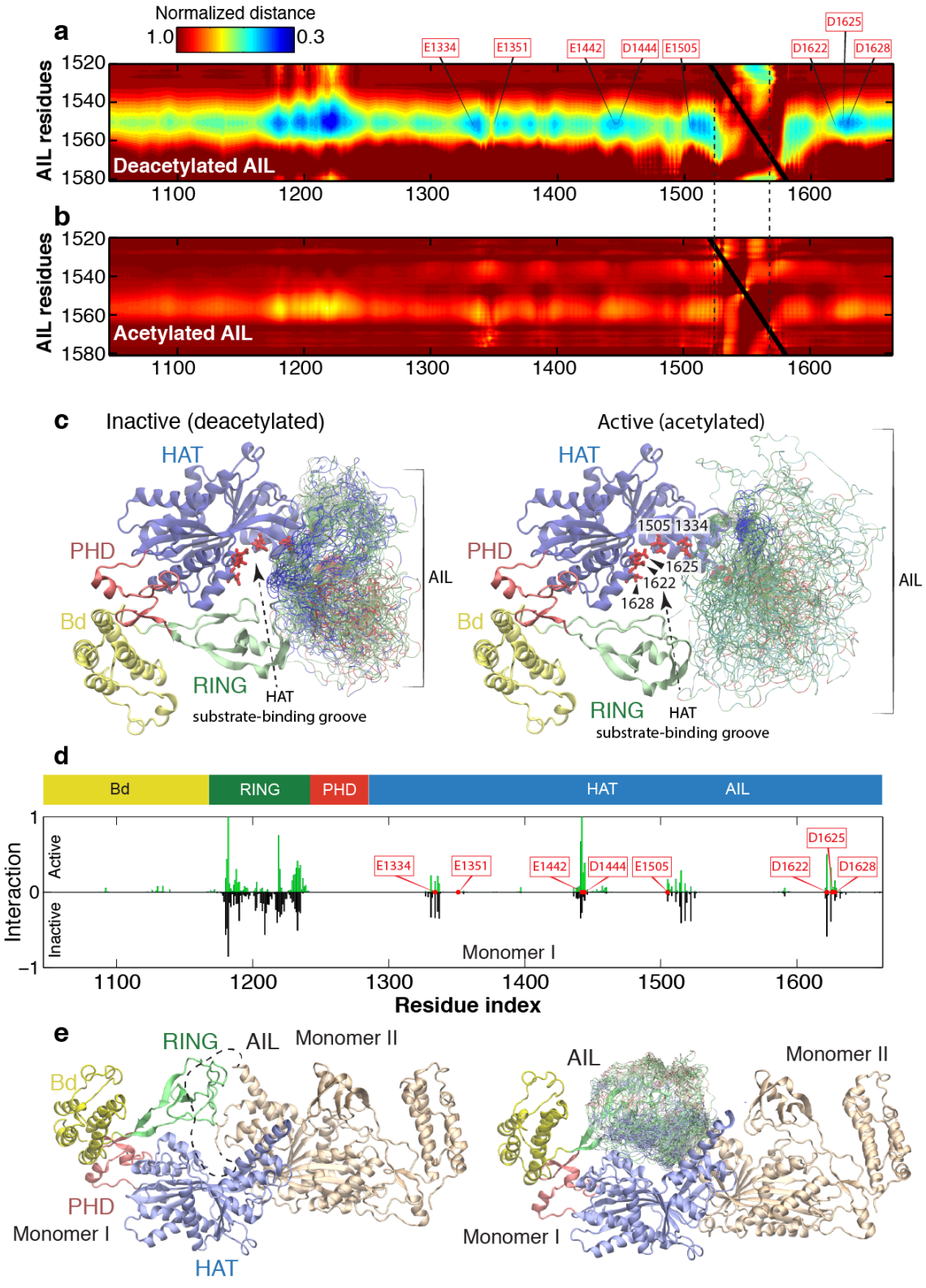
a
Normalized distance
1.0
0.3
E1334
E1351
E1442
D1444
E1505
D1622
D1625
D1628
AIL residues
1520
1540
1560
1580
Deacetylated AIL
1100
1200
1300
1400
1500
1600
b
AIL residues
Acetylated AIL
c
Inactive (deacetylated)
Active (acetylated)
HAT
PHD
Bd
RING
AIL
HAT
substrate-binding groove
1505
1334
1625
1622
1628
d
Bd
RING
PHD
HAT
AIL
Interaction
Active
Inactive
Monomer I
Residue index
e
RING
AIL
Monomer II
Bd
PHD
Monomer I
HAT

567

**Figure 5. Acetylation of the AIL regulates dynamic interaction with the substrate binding pocket of p300.** (**a**) Normalized distance between the AIL and residues in the inactive monomer. Inter-residue distances are normalized by the distances expected if the AIL behaved as a self-avoiding random coil. Electrostatic interaction mediated by conserved lysine residues between K1542 and K1560 of the AIL and aspartic/glutamic acid residues around the active site of the HAT domain, as shown by the residues highlighted (E1334, E1351, E1442, D1444, E1505, D1622, D1625, and D1628). The extensive contacts between the AIL and the RING domain originates in part from the RING domain's proximity to the AIL in its inactive conformation. (**b**) Normalized distance between the AIL and all residues in the active (acetylated) monomer. After acetylation, lysine-mediated electrostatic interactions are lost. (**c**) Representative conformations with the AIL shown as an ensemble for the inactive deacetylated monomer (left) and the active acetylated monomer (right). The Cα atoms of residues in the AIL are colored according to charge: blue (positive), red (negative) and green (non-charged). The HAT substrate-binding groove is more exposed in the active acetylated state, due to both the relative position of the RING domain and the lack of preferential interactions by the AIL. (**d**) Inter-molecular interactions in the loop-swapped dimer between the AIL of one HAT and the adjacent subunit of the other. The adjacent subunit is either in the active (top) and inactive (bottom) conformation. In the active state, the AIL is able to directly engage with residues E1442 and E1444 from the adjacent HAT substrate binding groove, suggesting the position of the RING domain has a steric impact on the accessibility of the AIL. **(e)** Simulations of the AIL in context of the loop-swapped dimer. Left panel: Cartoon of the trajectory of the AIL (dashed line). Right panel: Representative conformations with the AIL Cα backbone atoms are colored according to charge as in panel (B).

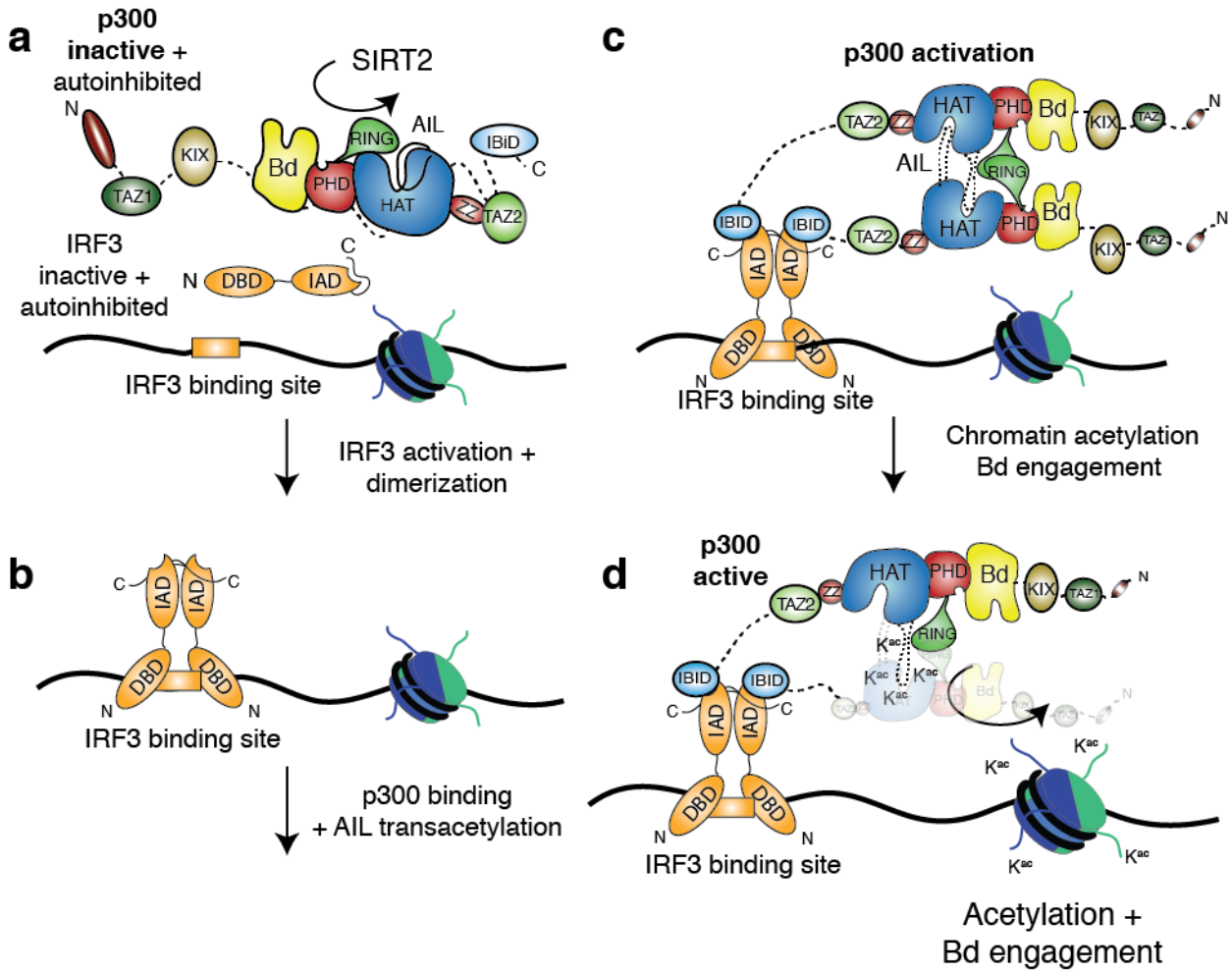


590

591 **Figure 6: Molecular model for p300 activation and DNA targeting. (a)** p300 is maintained in the
592 inactive state by deacetylases such as SIRT2. IRF3 is autoinhibited by a C-terminal segment in the IAD
593 domain. **(b)** TBK1 phosphorylation activates and dimerizes IRF3. The activated IRF3 dimer engages the
594 IBID domain of p300. **(c)** Recruitment of two copies of p300 results in trans-autoacetylation in the AIL
595 loop and HAT activation. **(d)** Activated p300 can acetylate chromatin and engage acetylated substrates
596 via the Bd.

597

598

599 **Table 1:** Summary of SEC-MALLS and mass spectrometry experiments

| Sample | $MM_{MS}$ Da | $MM_{th}$ Da | Acetylation level | $MM_{SLS}$ Da (2 mg·ml$^{-1}$) |
|---|---|---|---|---|
| BRP_HAT | 73538 | 73538 | ~0 | 73380 ±1.5% |
| BRP_HAT Acetyl | 73918 | 73538 | >8 | 71690 ±1.6% |
| BRP_HAT_CH3 | 92893 | 92891 | ~0 | 92810 ±2.0% |
| BRP_HAT_CH3 Acetyl | 93270 | 92891 | >9 | 90700 ±2.0% |
| BRP_HAT_CH3 ΔAIL | 86363 | 86362 | ~0 | 84650 ±2.2% |
| BRP_HAT_CH3 ΔAIL Acetyl | 86446 | 86362 | >2 | 80450 ±1.7% |

600 Column labeling: Molar masses determined by Mass spectrometry ($MM_{MS}$), $MM_{th}$ the theoretical molar
601 mass calculated from the appropriate primary sequences. Acetylation levels were estimated based on the
602 mass differences as compared to the non-acetylated sample. $MM_{SLS}$ (Molar masses determined by SEC-
603 MALLS) at a concentration of 2 mg·ml$^{-1}$. All p300 constructs contained the mutation Y1467F. The errors
604 reported for SEC-MALLS are the residual standard deviations of the observed data from the fitted values
605 calculated using Astra.

606

## Methods

### Constructs

For cell-free protein expression, cDNA of p300 (NCBI reference sequence: NM_001429.3) variants were cloned into the pIVEX2.4d vector (Roche) with a N-terminal 6x His tag and a C-terminal FLAG tag. In the ΔR constructs, the RING domain encompassing residues 1169–1241 was replaced by Glycine amino acid residue linker. In the ΔAIL constructs, loop amino acid residues comprising residues 1520–1581 were replaced by the flexible linker sequence SGGSG. For *E.coli* expression, cDNA encoding residues 1048-1282, for the BRP or BPΔR were cloned into the vector pETM-33 (EMBL) with a TEV cleavable N-terminal glutathione S-transferase (GST) tag. p300 BRP_HAT variants were cloned into pFASTBAC1 (Thermo Fisher) and expressed in insect cells as shown earlier[29]. p300s constructs, spanning amino acid residues 324-2414, were cloned into pFASTBAC1 vector with an N-terminal FLAG tag. HA-tagged full-length p300 variants were cloned into pcDNA3.1 (Thermo Fisher). Point mutations were introduced by QuikChange mutagenesis (Agilent). Point mutations and nucleotide deletions carried out in p300FL (1-2414) or p300s (324-2094) were done through transfer vectors as described previously[29]. STAT1ΔN (136-748), STAT1ΔNC (136-713) and IRF3ΔC (1-382) with a C-terminal intein tag were cloned into the pTXB1 vector (New England Biolabs) using the restriction enzymes *NdeI* (STAT1) or *NcoI* (IRF3) and *SpeI*. IRF3 (1-427) with an N-terminal His-tag cleavable by TEV protease was cloned using the restriction enzymes *NcoI* and *XhoI* into the vector pETM-11 (EMBL). All constructs were confirmed by DNA sequencing.

### Expression and Purification

Expression and purification of FLAG-tagged p300s constructs was done as described previously[2]. This method allows purification of p300s variants that are already preacetylated. Expression and purification of p300 BPR_HAT and SIRT2 were done as described in[29]. TBK1 was expressed in insect cells and purified

631 as described previously[21]. Cell-free protein synthesis was done in a 50 μL reaction volume. Briefly, 10 μg
632 $mL^{-1}$ of His-p300 variants in pIVEX2.4d were added to a reaction mixture containing 1 mM amino acid
633 mix, 0.8 mM rNTPs (guanosine-, uracil-, and cytidine- 5' triphosphate ribonucleotides), 1.2 mM
634 adenosine 5'-triphosphate, 55 mM HEPES, pH 7.5, 68 μM folinic acid, 0.64 mM cyclic adenosine
635 monophosphate, 3.4 mM dithiothreitol, 27.5 mM ammonium acetate, 2 mM spermidine, 5 μM ZnCl2, 80
636 mM creatine phosphate, 208 mM potassium glutamate, 16 mM magnesium acetate, 250 μg $mL^{-1}$ creatine
637 kinase, 27 μg $mL^{-1}$ T7 RNA polymerase, 0.175 μg $mL^{-1}$ tRNA, and 67 μL $mL^{-1}$ S30 E. coli bacterial
638 extract. Incubation was carried out at 22 °C with agitation for 16 h. Proteins were purified using Ni-NTA
639 chromatography (IMAC Sepharose 6 FF, GE healthcare) in buffer 1 (20 mM TRIS, pH 8.0, 300 mM
640 NaCl, 1 mM DTT, 5 μM $ZnCl_2$) containing Complete Protease Inhibitors EDTA-Free (Roche). The resin
641 was washed with 20 CV of buffer 1 and the protein eluted with 5 CV buffer 1 containing 300 mM
642 Imidazole. The protein was concentrated in a prewashed Amicon Ultra 0.5 ml Ultracel 10K Centrifugal
643 filter (Molecular weight cut off = 10kDa; EMD Millipore). The protein was buffer exchanged into buffer
644 1 using 0.5 ml Zeba Spin desalting columns (Molecular weight cut off = 7kDa; Thermo Scientific), flash
645 frozen in liquid $N_2$ and stored at -80 °C.

646 For expression of GST-BRP and GST- BPΔR fusion proteins in *E. coli* BL21 (DE3), LB medium
647 enriched with 100 μM $ZnCl_2$ was used. Cell pellets were resuspended in buffer 1 containing Complete
648 Protease Inhibitors EDTA-Free (Roche) and lysed by using a Microfluidizer (Microfluidics Corp., MA,
649 USA). The lysate was clarified by centrifugation for 30 minutes at 39,000 *g* in a JA-25.5 rotor (Beckman)
650 and applied to a Glutathione Sepharose 4 Fast Flow resin according to instructions by the manufacturer
651 (GE Healthcare). The resin was washed with buffer 1 and incubated with His-tagged TEV protease (1:100
652 w/w) for 14-16 h at 4°C. Subtractive Ni-NTA chromatography (IMAC Sepharose 6 FF, GE Healthcare)
653 was then employed to remove the residual His-tag and TEV protease. The untagged protein was further
654 purified by gel filtration on a High Load 16/60 Superdex 75 column (GE Healthcare) equilibrated in 20
655 mM HEPES, pH 7.5, 300 mM NaCl, 0.5 mM TCEP and 5 μM $ZnCl_2$. The final protein was concentrated

to 15 mg/ml in a prewashed Amicon Ultra-15 Centrifugal filter (Molecular weight cut off = 10kDa; EMD Millipore), flash frozen in liquid $N_2$ and stored at -80 °C.

The expression and purification of non-phosphorylated STAT1 variants (STAT1ΔN, STAT1ΔNC) and IRF3ΔC (1-382) was done in *E.coli* using the IMPACT expression system (New England Biolabs). For the expression of Y701 phosphorylated variants (pSTAT1ΔN, pSTAT1ΔNC), proteins were co-expressed with Elk receptor tyrosine kinase domain in *E.coli* BL21(DE3) TKB1 cells (Agilent). Cells were harvested by centrifugation and resuspended in buffer 2 (20 mM HEPES pH 7.5, 500 mM NaCl). The cells were lysed in a microfluidiser (Microfluidics Corp., MA, USA) and the soluble fraction was obtained by centrifugation for 30 minutes at 39,000 *g* in a JA-25.5 rotor (Beckman). The supernatant was first passed over chitin beads (New England Biolabs) and washed with buffer 2 for 10 column volumes. The protein was cleaved at 4°C for 16h in buffer 2 containing 50 mM DTT, eluted and further purified by gel filtration on a High Load 16/60 Superdex 200 column (GE Healthcare) equilibrated in buffer 2.

GST-STING, comprising the soluble cytoplasmic domain spanning amino acids 138-378, was expressed in *E.coli* BL21(DE3) at 37°C for 3 h. The cells were harvested by centrifugation and resuspended in buffer 3 (20 mM TRIS, pH 8.0, 300 mM NaCl, 1 mM DTT) containing Complete Protease Inhibitors EDTA-Free (Roche). The cells were lysed in a microfluidiser (Microfluidics Corp., MA, USA) and the soluble fraction was obtained by centrifugation as above. The supernatant was passed over equilibrated Glutathione Sepharose 4 Fast Flow resin according to instructions by the manufacturer (GE Healthcare). The resin was washed with buffer 3 and eluted with 10 mM reduced Glutathion in buffer 3. The protein was further purified by gel filtration on a High Load 16/60 Superdex 200 column (GE Healthcare) equilibrated in 20 mM HEPES, pH 7.5, 300 mM NaCl, 0.5 mM TCEP. The final protein was concentrated to 16 mg/ml in a prewashed Amicon Ultra-15 Centrifugal filter (Molecular weight cut off = 30 kDa; EMD Millipore), flash frozen in liquid $N_2$ and stored at -80 °C.

679 IRF3 was expressed in *E.coli* BL21(DE3) at 18°C for 16 h. The cells were harvested by centrifugation
680 and resuspended in buffer 2 containing 10 mM imidazole. The cells were lysed in a microfluidiser
681 (Microfluidics Corp., MA, USA) and the soluble fraction was obtained by centrifugation as above. The
682 supernatant was passed over $Ni^{2+}$–conjugated IMAC sepharose resin (GE Healthcare) and washed with
683 buffer 2 containing 20 mM imidazole. The protein was eluted in buffer 2 containing 500 mM imidazole
684 and was further purified by gel filtration on a High Load 16/60 Superdex 200 column in buffer 2
685 containing 0.5 mM TCEP. IRF3 was phosphorylated *in vitro* at a 1:10 molar ratio TBK1:IRF3 (1mg/ml)
686 in presence of 5 mM $MgCl_2$ and 1 mM ATP. The reaction was incubated at 30°C for 1h and then for an
687 additional 10h at 21°C. Phosphorylated IRF3 was further purified by size exclusion chromatography on a
688 Superdex S200 16/60 column (GE Healthcare) in 20 mM HEPES, pH 7.5, 300 mM NaCl, 0.5 mM TCEP.
689 The production of recombinant histones was done following standard procedures[54].

690

691 **Crystallization and structure determination**

692 The p300 BRP_HAT construct comprising the AIL and the mutation Y1467F was deacetylated as done
693 previously[29]. The protein at 4.5 mg $ml^{-1}$ was incubated with a three-fold molar excess of the bi-substrate
694 inhibitor Lys-CoA[34] prior to crystallization. Crystals in the $P2_1$ space group were grown by hanging-drop
695 vapor diffusion at 4 °C by mixing equal volumes of protein and crystallization solution containing 100
696 mM HEPES, pH 7.5, 18-22% polyethylene glycol 3350, 0.2 M NaCl. Crystals were cryoprotected in 20-
697 25% ethylene glycol and drop frozen in liquid nitrogen. We collected native diffraction data to a
698 minimum Bragg spacing of 3.1 Å resolution at the ESRF on beamline ID29 under a nitrogen gas stream at
699 100 K, at a wavelength of 1.282 Å. We processed the data with XDS (Extended Data Table 1). The
700 structure of the p300 BRP_HAT was determined by molecular replacement using Phaser. There are four
701 copies in the asymmetric unit and the RING domains were initially not visible in the electron density map
702 and are partially disordered. Inspection of an anomalous difference map indicated peak density for the

zinc ions and allowed positioning of the RING domain in the outward rotated conformation. A final model was produced by iterative rounds of manual model building in Coot and refinement using PHENIX. The final model contains residues 1045 -1664 with a deletion of residues 1534-1567 and was refined to a 3.1 Å resolution with an $R_{work}$ and an $R_{free}$ of 19% and 26%, respectively (Extended Data Table 1). Analysis of the refined structure by MolProbity showed that there are no residues in disallowed regions of the Ramachandran plot. The MolProbity all atom clash score was 1.91, placing the structure in the 100$^{th}$ percentile among structures refined at 3.1 Å resolution (N=2108).

The BPΔR construct at 15 mg ml$^{-1}$ was mixed with 2 mM of a 11-mer histone peptide H4 (10-20) GLGKacGGAKacRHR (only the underlined amino acid sequence is visible in the electron density map) containing two acetylated Lysine residues at positions K12 and K16 (H4K12K16). Crystals in the $P2_12_12_1$ space group were grown by hanging-drop vapor diffusion at 21°C by mixing equal volumes of protein and crystallization solution containing 1.6 M Ammonium Sulfate, 100 mM Bicine, pH 9.0. Crystals were cryoprotected in 20% ethylene glycol and drop frozen in liquid nitrogen. We collected native diffraction data to a minimum Bragg spacing of 2.5Å resolution at the ESRF on beamline ID29 under a nitrogen gas stream at 100K, at a wavelength of 1.0Å (Extended Data Table 1). Data processing, molecular replacement and refinement were done as indicated above. The final model contains two copies of the BPΔR module corresponding to residues 1049 -1279 of p300 in the asymmetric unit. As expected, replacement of the RING domain residues 1169-1241 by a single Glycine amino acid linker did not adversely affect the remainder of the BP module. Analysis of the refined structure by MolProbity showed that there are no residues in disallowed regions of the Ramachandran plot. The MolProbity all atom clash score was 0.97 placing the structure in the 100$^{th}$ percentile (N=6960).

**Monte Carlo simulations**

All-atom Monte Carlo simulations were performed using ABSINTH implicit solvent model and version 2 of the CAMPARI Monte Carlo simulation engine (http://campari.sourceforge.net)[33]. The initial AIL loop was constructed using MODELLER, and the complete set of backbone and side chain torsional angles were sampled for the AIL for which electron density was missing. Simulation analysis was performed with MDTraj and CTraj (http://pappulab.wustl.edu/CTraj.html)[55]. The backbone degrees of freedom of the folded domains were not sampled, while all amino acid side chains were fully sampledCAMPARI simulations explore conformational space through perturbation to the torsional angles (as opposed to Cartesian positions, as is typical for molecular dynamics). Consequently, a fully closed loop represents a major sampling challenge. To address this, we severed the covalent backbone bond between the N-terminal part of the AIL loop and the folded domain, and replaced this bond with a strong harmonic potential that recapitulates the distances constraint associated with the covalent bond. This allows moves to fully rotate the chain and dramatically improves the efficiency of conformational sampling.

We generated 5000 independent non-overlapping starting configurations and used a clustering approach to identify the most distinct 200 conformations. These were used as the starting conformations for full simulations. We ran 200 independent simulations of the deacetylated and acetylated p300 in the monomeric form, and 200 independent simulations of the loop-swapped p300 dimer in the active and inactive form (800 simulations total). Analysis was performed after an initial equilibration. Dimer simulations applied a harmonic potential between residue 1550 from the AIL and residue 1442 from the other monomer to maintain the AIL in the active site. This allowed us to directly compare active site accessibility of the AIL. For monomer simulations, no restraints were applied.

Each residue on the folded structure was evaluated for contacts with any residue in the AIL, and these contacts were summed to give an effective contact score. In this manner, the residues on the folded structure that most frequently interacted with any residue on the AIL were directly identified. Interaction was primarily of electrostatic nature, with residues E1334, E1444, E1505, D1622, D1625 and D1628 engaging in direct interactions. There are also extensive interactions between the AIL and the RING

751 domain, although we cannot rule out that these interactions are driven by the harmonic applied to pull
752 E1442 towards the active site. As might be expected, the AIL-RING interactions differed between the
753 active and inactive conformation.

754 To assess interactions between the AIL and the folded domains in the monomer simulations scaling map
755 analysis was performed. In this analysis, a simulation of the AIL as a true self-avoid random coil is
756 performed to generate a reference state, and then the mean inter-residue distances obtained in the full
757 simulations are normalized by the distances obtained from this reference. The self-avoiding random coil
758 simulations are performed using an identical protocol to the full simulations, with the notable exception
759 that all attractive interactions between atoms or solvation effects, instead using only the repulsive part of
760 the Lennard-Jones potential. This ensures we generate a sequence and structure-specific self-avoiding
761 random coil ensemble that provides a true reference state. Extensive details on the technical aspects
762 associated with the generation of this reference state have been described previously[56]. The scaling maps
763 allow us to easily identify local regions that engage in interactions that cause deviations from self-
764 avoiding random coil behavior.

765

766 **HAT assays**

767 The standard autoacetylation HAT assay was done using $^{14}$C-acetyl-CoA (Perkin-Elmer). Autoacetylation
768 of p300 was quantified by autoradiography after SDS-PAGE gel analysis. The p300s preparations were
769 equilibrated in 1x HAT buffer (25 mM TRIS-HCl, pH 7.5, 100 mM NaCl, 1 mM DTT, 10% glycerol and
770 1x Complete EDTA-free protease inhibitor (Roche)) for 10 min at 30°C prior to initiation of the reaction
771 by the addition of 200 μM $^{14}$C-acetyl-CoA for the indicated time points. For experiments containing IRF3
772 STAT1 or the eRNA Klf6, autoacetylation assays were performed at a fixed equimolar concentration (2
773 μM) of p300s and the indicated TF or Klf6. Assays were performed in triplicates with different batches of
774 proteins and on different days. At the indicated time point, 5 μl of the reaction was quenched by addition

of 5 µl of 2x SDS gel loading buffer followed by analysis on a 4-20% SDS-PAGE gel. Experiments shown in Fig. 1d were done in 1x kinase buffer (20 mM HEPES, pH 7.5, 250 mM NaCl, 20 mM β-glycerol phosphate, 1 mM sodium vanadate, 10 mM $MgCl_2$, 1 mM DTT, 1 mM ATP and a mix of 20 µM [$^{14}$C] acetyl-CoA and 80 µM cold acetyl-CoA (A2056, Sigma). 1 µM of p300s was incubated in the presence or absence of 1 µM IRF3, 2 µM TBK1 and 1 µM STING (lanes 1-6) or increasing amounts of STING as indicated (lanes 7-12). The gels analyzed by western blotting as indicated below or were fixed for 30 min in a solution containing 3% glycerol, 10% glacial acetic acid, 20% ethanol (v/v/v) in water. The gels soaked for 5 min in a solution containing 1% glycerol, 5% PEG8000 in water and were dried for 30 min using a Bio-Rad Gel Dryer and the radioactivity quantified on a phosphorimage analyser (Typhoon, GE Healthcare) followed by analysis using imageJ 1.8.0_112[57].

A p300 HAT scintillation proximity assay (SPA) was designed similar to that described previously[22]. Briefly, as a substrate we used a synthetic histone H4 peptide containing 15 amino acids derived from the N-terminus of human H4 that was chemically attached to biotin with an amino hexanoic linker (Biotin-C6- GRGKGGKGLGKGGAK) (from peptid.de). The synthetic peptide was re-suspended in water and adjusted to pH 7.0 with concentrated NaOH.

A typical reaction contained p300s (50 nM), 12.5 µM biotinylated H4 peptide, acetyl-CoA (0.1 µM to 10 µM set at ~10x apparent Km) in 20 mM Tris-HCl, pH 8.0, 150 mM NaCl, 5 µM $ZnCl_2$, 0.01% Tween-20, 0.1% BSA (w/v). For reactions containing pIRF3, 50 nM was added. 20µl of a 2x reaction mixture containing p300s, H4 peptide with and without pIRF3 was preincubated at 30°C for 5 min. The reaction was initiated by the addition of 20 µl of 2x acetyl-CoA containing a 1:3 mix of Tritiated [$^3$H] acetyl-CoA (PerkinElmer; NET290050UC) with cold acetyl-CoA. Eg. for 10 µM final acetyl-CoA concentration, a mix of 5 µM [$^3$H] acetyl-CoA and 15 µM cold acetyl-CoA (A2056, Sigma) was used. The reaction was quenched at the indicated time points by delivering 40 µl of the reaction mix into 120µl of 0.5N HCl in a FlashPlate Plus Streptavidin 96-well scintillant coated microplate (Perkin Elmer, SMP103001PK). The

plate was incubated for 1h, and light emission was counted in a MicroBeta2 Scintillation Counter (Perkin Elmer) at 1 minute per well in the top count mode. Counts per minute (cpm) were plotted against acetyl-CoA concentration. Typical progress curves are shown in Extended Data Fig.1d. The initial rate was estimated by linear regression during the first 10 minutes of the reaction and plotted against acetyl-CoA concentration. All data were analyzed using GraphPad Prism 7.0.

For results shown in Fig. 4, acetylation reactions, were performed in acetylation reaction buffer HAT (25 mM TRIS-HCl, pH 7.5, 100 mM NaCl, 0.1 mM EDTA, 1 mM DTT, 10 % glycerol and 1× Complete EDTA-free protease inhibitor (Roche)) with 50 µM Acetyl CoA (Sigma), 100 ng/ml TSA and 2 µg of purified histone octamer. Reactions were incubated 30 min at 30 °C and stopped by addition of 3x SDS gel loading buffer, then used for Coomassie staining and Immunoblotting.

**Multi angle laser light scattering-size exclusion chromatography.**

Prior to SEC-MALLS runs, p300 variants were acetylated and deacetylated using p300 HAT or SIRT2 as described previously[29]. The reactions were analyzed by liquid chromatography-mass spectrometry (LC-MS) as done previously[58]. Size-exclusion chromatography was performed at a flow rate of 0.5 ml $min^{-1}$ on a Superdex 200 Increase 10/300 GL column equilibrated in SEC-MALLS buffer (20 mM HEPES, 300mM NaCl, 5µM $ZnCl_2$, 0.5mM TCEP) at 21 °C. A 50 µl sample of p300 at 2 mg $ml^{-1}$ was injected onto the column and multi angle laser light scattering was recorded with a laser emitting at 690 nm using a DAWN-EOS detector (Wyatt TechnologyCorp. Santa Barbara, CA). The refractive index was measured using a RI2000 detector (Schambeck SFD). The molecular weight was calculated form differential refractive index measurements across the center of the elution peaks using the Debye model for protein using ASTRA software version 6.0.5.3.

**In vitro eRNA transcription**

eKlf6 eRNA corresponding to 496 nucleotides of the sense strand of human chr13:5802100-5802596[38], was produced by in vitro transcription from a pMA plasmid containing a eKlf6 insert synthesized by GeneArt Gene Synthesis (Thermo Fisher). 50 µg of pMA_Klf6 plasmid was linearized with 80 U of *Kpn*I-HF in a final volume of 100 µl and incubated at 37 °C for 14-16h. The *in vitro* transcription reaction was done in a final volume of 1 ml, using 1x T7 buffer , T7 RNA Polymerase and 1 U of RNaseOUT Recombinant Ribonuclease Inhibitor (Thermo Fisher). After incubation for 2 h at 37°C, 0.5 U of TURBO™ DNase (2 U/µl) (Thermo Fisher) and 1µM $CaCl_2$ was added to the reaction and incubated for 30 min at 37 °C. Following DNase treatment, 2 µl of a 30 mg/ml stock of proteinase K powder (Thermo Fisher), dissolved in proteinase K buffer (10 mM TRIS pH 7.5, 1 mM $CaCl_2$, 40% Glycerol), was added and incubated for 45 min at 37 °C. Buffer was exchanged into 20 mM HEPES, pH 7.5, 300 mM NaCl, 0.5 mM TCEP using Amicon Ultra-0.5ml Centrifugal Filters (Molecular weight cut off = 3kDa; EMD Millipore). To further purify the RNA, 3 volumes of TRIzol (Thermo Fisher) was added to the RNA sample, followed by isopropanol precipitation. Purified eKfl6 RNA was resuspended in 20 mM HEPES, pH 7.5, 300 mM NaCl, 0.5mM TCEP. RNA was quantified using a Nanodrop spectrophotometer (Thermo Fisher). The quality of Klf6 was assed by agarose gel electrophoresis in 1x TBE buffer or using denaturing 6M Urea 14% PAGE (Extended Data Fig. 7c).

**Immunoblotting, Immunofluorescence and antibodies**

For immunoblotting, proteins were separated on 4–12% Bis-Tris SDS-PAGE gel (NuPAGE precast gel, Thermo Fisher) and transferred onto a nitrocellulose membrane (Hybond C+, GE Healthcare). Membranes were blocked with 5% skim milk in PBST buffer (PBS, 0.1% Tween-20) and probed with anti–p300 K1499ac rabbit polyclonal antibody (1:2,500 dilution; Cell Signaling, 4771), anti-Kac rabbit polyclonal antibody (1:2,500 dilution; Cell Signaling, 9441), anti-Flag mouse monoclonal antibody

(1:2,500 dilution; Sigma, F1804), anti-HA rabbit polyclonal antibody (1:2500 dilution, Abcam, ab9110). For the detection of STAT1 or IRF3 phosphorylation, the membrane was blocked with 5% milk in PBST followed by overnight incubation at 4 °C with anti-phospho-Stat1 (Tyr701) Rabbit monoclonal antibody (1:2,500 dilution; Cell Signaling #9171) in PBST buffer containing 5% bovine serum albumin (BSA). For detection of IRF3 S396 phosphorylation, we used anti-phospho IRF3 S396 Rabbit monoclonal antibody (1:2.500 dilution; Cell Signaling #4947). Incubations were done as above. Membranes were washed extensively in PBST buffer before and after incubation with anti-rabbit or anti mouse HRP-conjugated secondary antibody (1:10,000 dilution; GE Healthcare, NA934 or NA931), and protein bands were visualized on film after the ECL reaction (ECL Prime, GE Healthcare). Immunofluorescence was done as described previously[29] or as follows: 24h post-transfection, cells were treated with a DMSO control or with 2.5µM (final concentration) of HAT inhibitor A-485 (Phil Cole, Harvard Medical School) or CBP/p300 Bromodomain inhibitor (CBP30, Sigma # SML1133) dissolved in DMSO. The final DMSO concentration in all assays was 0.25%. After 24h, Cells were rinsed once with RNase-free PBS 1X. Next, cells were permeabilized in freshly made 0.2% Triton (SIGMA) buffer for 5 min and were then fixed in freshly made 4% formalin solution (SIGMA) for 10 min at room temperature. After three washes in RNase-free 1x PBS at room temperature, the cells were incubated in 5% skim milk in 1x PBS for 30 min and then probed with anti-HA high-affinity monoclonal antibody (1:100 dilution; Roche Applied Science, cat N°:11867423001) overnight at 4°C. Cells were washed extensively with 1x PBS before and after incubation with Alexa Fluor 488-conjugated secondary antibody (1:500 dilution; Invitrogen, Cat N°:A-11006) for 1h at 37°C. Cells were counterstained with Hoechst (250ng $ml^{-1}$) and examined under a confocal laser scanning microscope (LSM510, Zeiss).